RESEARCH PAPER

Correlations of the capture efficiency with the Dean number and its constituents in heterogeneous microfluidic immunosensors

Shipra Verma[1,2] · Siddhartha Panda[1,2,3]

Abstract

In heterogeneous microfluidic immunosensors, enhanced *capture efficiencies* of the antigens (Ag) in the carrier fluids by the surface-immobilized antibodies (Ab) facilitate lower detection limits and thus early detection of disease. *Capture efficiency* depends on the interplay of transport, reaction parameters and the geometry of the system. A detailed analysis on the enhanced *capture efficiencies* due to secondary flows in heterogeneous immunosensors has not received significant attention and is the theme of the present work. We conducted a systematic study to observe the significance of secondary forces on the *capture efficiency,* manifested as the average surface concentration ($C_{s,\text{avg}}$), in serpentine channels of different lengths (l) and radius of curvature (R_c) as a function of the Reynolds number (*Re*). Experimental observations were validated with numerical simulations. Micro-PIV studies at different planes and sections of the serpentine microchannels were conducted and matched with the simulated velocity profiles. Further investigation of the process and the geometrical parameters was conducted using numerical simulation and the behaviour of $C_{s,\text{avg}}$ as a function of *Re* and R_c was plotted for different cases. A highlight of the present work are correlations of $C_{s,\text{avg}}$ as a function of the Dean number (*De*), as well as its constituents (*Re* and α). The scientific studies of the geometrical and process parameters which affect the analyte capture advance the understanding of the phenomena and the proposed engineering correlations would be useful in the design of more efficient flow-based heterogeneous immunosensors.

Keywords Microfluidic immunosensor · Capture efficiency · Dean number · Secondary flow · Figure of merit

1 Introduction

In heterogeneous microfluidic immunosensors, antibodies are immobilized on the channel walls via intermediate linkers, and the sample containing the antigens flows through the microchannel. Here the term "heterogeneous" indicates that the *antibodies* (Ab) and *antigens* (Ag) are present in

✉ Siddhartha Panda
  spanda@iitk.ac.in

[1] Department of Chemical Engineering, Indian Institute of Technology Kanpur, Kanpur, UP 208016, India

[2] Samtel Centre for Display Technologies, Indian Institute of Technology Kanpur, Kanpur, UP 208016, India

[3] National Centre for Flexible Electronics, Indian Institute of Technology Kanpur, Kanpur, UP 208016, India

different phases (Rath et al. 2012; Rath and Panda 2015a, b, 2016; Lynn et al. 2014; Squires et al. 2008). The antigens are transported from the bulk solution to the surface where they react (bind) with the antibodies, and are thus captured. One performance parameter of a flow-based heterogeneous immunosensor is its "*capture efficiency*", which is defined as the ratio of the amount of antigens captured to the maximum available antibodies on the immunosensor surface (Rath et al. 2012; Rath and Panda 2015a). A higher *capture efficiency* manifested in higher average surface concentration ($C_{s,\text{avg}}$) of the bound antigens will reduce the limit of detection (LOD) and facilitate early disease detection. As the capture of the antigens occurs sequentially through the steps of transport and reaction, efforts to enhance the *capture efficiency* have focused on these two areas. *Capture efficiency* has been enhanced by refining surface engineering, i.e., by physical modifications [such as surface texturing (Rath et al. 2012)], chemical modification such as site-directed proteins, and by modulation of process engineering parameters, e.g., using optimum pH and temperature, tuning

surface energies, and zeta potential, etc. (Rath and Panda 2015a, 2016; Chepyala and Panda 2013, 2014; Vijayendran and Leckband 2001; Squires et al. 2008; Hu et al. 2007; Nelson et al. 2007; Reverberi and Reverberi 2007; Lebedev et al. 2006; Ibii et al. 2010). *Capture efficiency* has also been enhanced by facilitating transport through mixing (both active and passive). Fluid travelling in a curved path is subjected to a centrifugal force which gives rise to a secondary flow and the magnitude of the force due to secondary flow has been characterized by a dimensionless number, the Dean number, $De = Re \cdot \alpha^{0.5}$ (Dravid et al. 1971), where Re is the Reynolds number and α is the ratio of the channel hydraulic radius (r) to the flow path radius of curvature (R_c).

The role of secondary flows has been studied in heterogeneous immunosensors with respect to the enhancement of mass transfer and the eventual analyte capture. The secondary flow is governed by the process parameters (such as the carrier fluid velocity) and the geometry parameters (such as the radius of curvature of the microchannel, groove width, height etc.). Several authors have studied the effect of these parameters (Foley et al. 2008; Golden et al. 2007; Lynn and Homola 2015; Lynn et al. 2015; Vijayendran et al. 2003; Wang et al. 2011; Kirtland et al. 2006; Jeon and Shin 2009) to enhance the extent of immunosensing in microchannels. Experimental studies for the effect of herringbone structures in channels have been reported; Foley et al. (2008) and Golden et al. (2007) compared the performance of the herringbone structured microchannels with straight microchannels and found enhanced immunosensing in the geometrically patterned microchannels attributed to the enhanced mass transfer effected by the transverse circulation. Jeon and Shin (2009) also studied various geometries of micromixers (with circular, rectangular, rhombic, contraction-enlargement, and zigzag obstructions) experimentally and numerically and obtained improved mixing and mass transfer, and proposed their use in bio-medical and immunosensing applications. Regarding the process parameters, Vijayendran et al. (2003) studied the binding rates in a serpentine microchannel and Wang et al. (2011) analyzed the impact of the flow rate at various areas along the channel length having herringbone structures; both reported an enhancement in the immunosensing (in the form of enhanced signal) when compared with the straight channels. Lynn et al. (2015) studied experimentally both the process and the geometrical parameters, and the analysis was supported by the simulation studies conducted by Lynn and Homola (2015) and Kirtland and Stroock. Kumar et al. (2011), Bange et al. (2005) and Hessel et al. (2005) reviewed the different methods to enhance mixing and the mass transfer coefficient due to the addition of secondary flows in micro-reactors including immunosensors. However, the analysis of the secondary flows in curved microchannels for immunosensing applications has not got sufficient attention. The effects of parameters on the mass transfer coefficient, boundary layer thickness along with any correlation between the surface concentration of the captured analyte and the parameters (process and geometrical) have not been reported in the literature, and an extensive study of the parameters of interest has not been done. This is the motivation of the present research which has a focus on obtaining the optimum process and geometrical parameters for a given system with regards to the analyte capture, along with the *figure of merit*, (*FOM*) (Mandal et al. 2011).

In this study, the effect of secondary flow on the capture efficiency in heterogeneous immunosensors was studied for the detection of prostate-specific antigens (PSA) molecules. Utilizing channels with a given rectangular cross-section and length, we used a straight microchannel as a base case and serpentine geometries as the test cases. We performed flow experiments to determine the *capture efficiency* at several flow rates. The extent of the analyte capture was analyzed with the help of micro-PIV (at different planes and locations in the microchannels) and numerical simulations were utilized to understand the capture mechanism. Using a diffusion–convection–reaction model, the dependences of the process parameters on the transport and reaction parameters was obtained. We also obtained different parameters such as average molar flux, boundary layer thickness (additional plots in supplementary information, Figs. S1 and S2), etc. A highlight of this work is the development of a correlation among process parameters, geometric parameters, and the average surface concentration of the captured antigens. There is a need for efficient designs which consider the effects of all the aforementioned parameters together with specific considerations for transport, reaction, and geometry of the immunosensor, and this study is an effort in that direction.

2 Experimental section

2.1 Chemicals

Chemicals used for experiments were obtained from different sources. PDMS was obtained from SYLGARD 184 (Dow Corning, USA), and glass slides were obtained from Bioplus (India). The constituents required for the PBS solution (KCl, NaCl, Na_2HPO_4, and KH_2PO_4) were obtained from Qualigens (India); the pH of PBS was maintained at 7.4 for all experiments. Mercapto Propionic Acid (MPA) and EDC-NHS for creating functionalizing group on the gold surface were purchased from Sigma Aldrich (Germany) and Merck (Germany), respectively; isopropanol (IPA) was purchased from Loba Chemie (India); potassium ferrocyanide and potassium ferricyanide were purchased from Rankem (India); SU-8 2050 epoxy for making moulds was obtained from MicroChem Corporation (USA); prostate-specific

antigen (PSA) was obtained from Fitzgerald Industries International (USA), anti-PSA antibodies were purchased from Genetech Laboratory (India), bovine serum albumin (BSA) and anti-BSA were obtained from Merck (India) and silicon wafers [(100), surface roughness < 2 nm] were purchased from Wafer World (USA).

2.2 Channel fabrication

Glass-PDMS channels were used as the flow channels. There is a large body of literature using such systems (Srivastava et al. 2011; Zhang et al. 2015; Chen et al. 2019; Meng-Di et al. 2019). The straight microchannels of length 10 mm [Fig. 1a(i)] and 20 mm (not shown) were taken as the base cases with height and width of 50 and 800 μm, respectively. For the serpentine microchannels, we use the unit of a semicircle with a 5 mm curved length; a design with two semicircles of length 10 mm [Fig. 1a(ii), called here as a one cycle serpentine microchannel] and another design with four semi-circles of total 20 mm length [Fig. 1a(iii), called here as a two cycle serpentine microchannel] were used. The serpentine microchannels have same width and height as the straight channels. All the process steps were performed in a controlled clean room environment. The glass slides were cleaned using Piranha solution (H_2SO_4:H_2O_2 :: 3:1) followed by rinsing with DI water and drying with N_2. Immediately after drying, chromium (thickness 10 nm) and gold (thickness 90 nm) of the required shapes (straight and serpentine), were deposited on the glass via thermal deposition, followed by annealing at 300 °C for 1 h. Experimentally, the presence of the Cr/Au in the bulk was confirmed using EDX (instrument Model no: JSM-6010LA, JEOL) and the presence of only gold at the interface with air was confirmed using XPS (instrument Model no: PHI 5000 Versa Probe II, FEI) (EDX and XPS, spectra have been given in the Supplementary Information, Figs. S3 and S4). The calculated diffusion lengths of Cr in Au under the conditions were far less than 90 nm, and this supported the experimental evidence of only gold on gold–air interface. Metal deposition masks as well as epoxy moulds were prepared using a laser system (Nd:YAG Laser, Laservall, Italy). PDMS flow channels were made using SU-8 epoxy-based on protocols reported in the literature (Di et al. 2019; Art et al. 2018; Kadilak et al. 2014; Fujii 2002). For fabrication of the epoxy mould, epoxy was spin-coated on silicon for consecutive steps at 500 and 2500 RPM for 10 and 45 s, respectively. The spun epoxy was prebaked for 7 min at 95 °C, exposed to a 240 mJ/cm² UV lamp with a copper mask for 8 min, followed by post-baking at 95 °C for 7 min. The baked epoxy was developed in SU-8 developer in 7 min. This was followed by washing with fresh developer for 10 s and with IPA for 15 s. In the next step, the PDMS mixture was prepared (base and cross linker) in 10:1 ratio (by weight), degassed, poured over the epoxy

moulds, and was cured at 70–72 °C for 1 h in vacuum. This was cooled and the PDMS channel was separated from the mould. The inlet/outlet ports were drilled and bonded to the gold-deposited glass slide using oxygen plasma. Thus, the microchannels were fabricated. For the micro-PIV study, we used a glass-PDMS channel without a gold layer to observe the flow profile as the gold layer blocked visual inspection of the flow profile. Figure 1b and c show the complete experimental setup and the microchannel with the flow set-up.

2.3 Channel functionalization

Figure 1d shows the stack immobilization and functionalization process steps, i.e., from the non-functionalized gold surface to the capture of PSA by anti-PSA (Fig. 1d(i)–(v)) on the straight microchannel (Bhuvana et al. 2013). The process steps are the same for the serpentine microchannels. In brief, it included the rinsing of the microchannel with ultrapure water, followed by drying with nitrogen, and subsequently, the channel surface (gold surface) was incubated in a 1 mM MPA solution in PBS solution for 2 h to form the SAMs (self-assembled monolayers), followed by thorough washing with PBS. The terminal carboxylic acid (–COOH) groups were activated, followed by immobilization of 0.2 M NHS/0.05 M EDC (1:1 mixture) for 4 h at room temperature. After rinsing with PBS, the channel was incubated overnight in a 100 μg/mL antibody solution. Finally, after rinsing with PBS, antigen (1 μg/mL) in PBS was flown through the microchannels for the Ab–Ag reaction. After every step, we thoroughly washed our microchannels to remove the adsorbed molecules from the PDMS surface (Li et al. 2009). Due to a leakage problem at higher flow rates, we limited our flow rates for experiments up to 50 μL/min and 30 μL/min in the 10 mm and 20 mm channels, respectively. Figure 1e and f show the top-down view of a part of the microchannel at 5X magnification, without any flow and with flow (of blue dye in water) at 50 μL/min; no change on the width indicates that the channel dimensions do not change under these flow conditions (no changes in the height were seen as well [images not shown here]). The range of *Re* corresponding to the said flow rate lies between 0.04 and 1.95, and similar range has been reported in the literature (Lynn et al. 2013).

2.4 Determination of capture efficiency

Cyclic voltammetry (CV) was performed after each stack immobilization and functionalization process to capture PSA by anti-PSA [Fig. 1d(i)–(v)] on the microchannels (straight as well as serpentine). 1 mM (1:1) solution of potassium ferrocyanide ($K_4[Fe(CN)_6]$) and potassium ferricyanide ($K_3[Fe(CN)_6]$), in 10 mM (pH = 7.4) PBS solution (Bhuvana et al. 2013; Imran et al. 2019a, b), was used as the electrolyte. Platinum was used as for the working
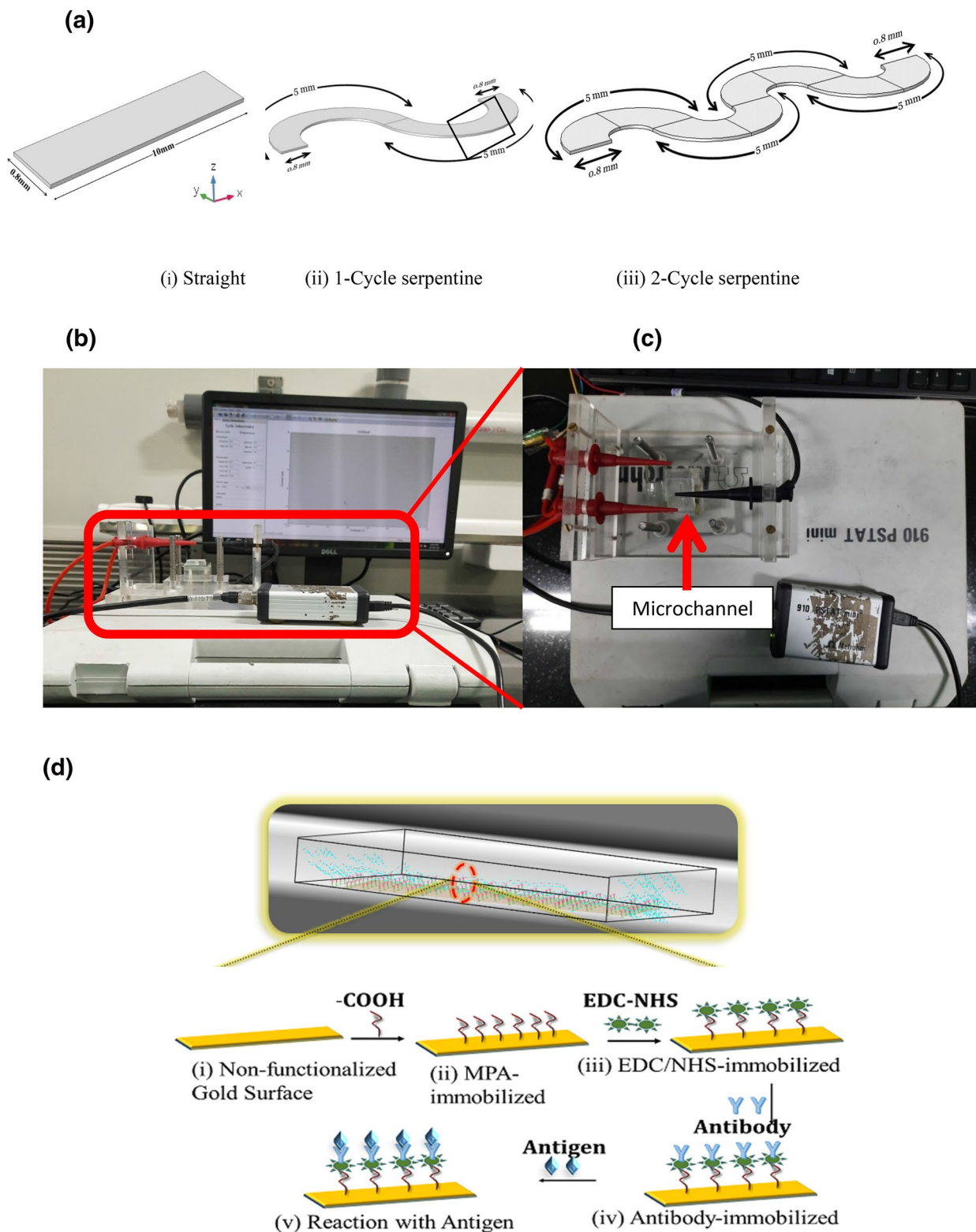
Fig. 1 **a** (i) Schematics of the straight (10 mm), (ii) 1-cycle serpentine (the highlighted boxed region in the microchannel, has been used for the micro-PIV study) (10 mm) and (iii) 2-cycle serpentine (20 mm) channels. **b** The experimental set-up, **c** Microchannel with the flow set up, **d** Schematic of the stack immobilization process for the capture of PSA by anti-PSA on the gold surface of the microchannel. **e** The top-down view of the microchannel at 5X magnification: before flow and, **f** after flow
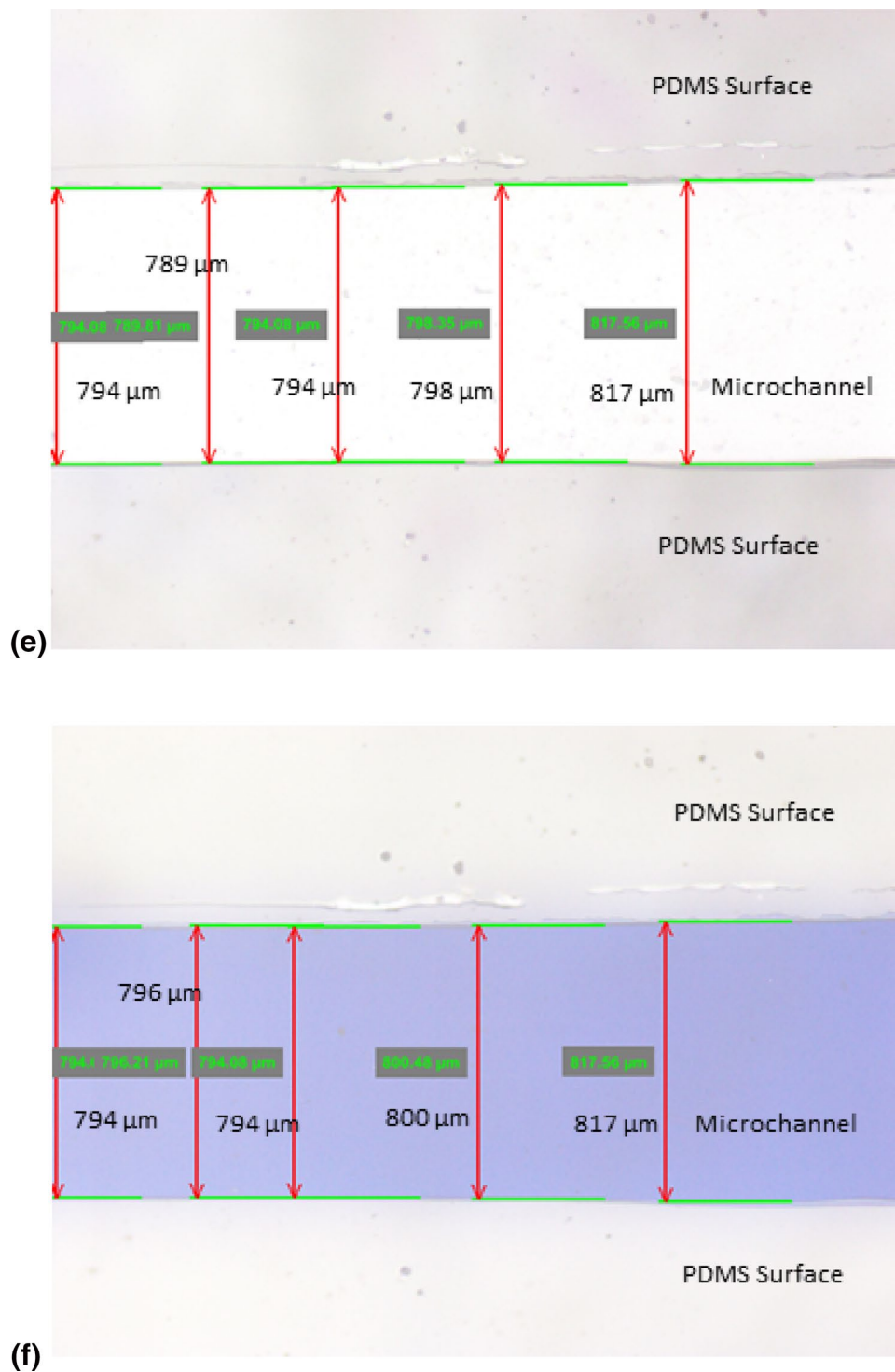
(e)

(f)

Fig. 1 (continued)

and counter electrodes and Ag/AgCl as the reference electrode (Zhang et al. 2019). Using the information from CV and the Brown-Anson model (Brown and Anson 1977), the number of active sites with respect to peak current were calculated as reported in the literature (Kalita et al. 2012; Klink et al. 2011; Singh et al. 2011; Solanki et al. 2008; Chauhan et al. 2016) and utilized in our work. A higher reduction in the value of the peak current, due to higher extent of reaction, indicated a lower number of active sites.

2.5 Flow characteristic using micro-PIV

The flow profiles inside the channel were analyzed by micro-PIV (TSI, USA) to characterize the flow profile. Studies were performed at flow rates 40–100 µL/min and different planes (bottom surface, an intermediate plane and the mid-plane) and sections (bend and U-turn section) within the serpentine microchannel.

2.6 Simulation technique

The procedure for simulating the PSA (Ab) capture is governed by the equations shown in the next Sect. (2.6.1). The computational method presented in this study made use of the finite element method (FEM) using COMSOL multiphysics software. The required modules were the "Navier–Stokes equations", "transport of dilute species" and "surface reactions". All modules were solved using the PARDISO solver. We could not go beyond a channel length of 10 mm due to computational limitations.

2.6.1 Governing equations

The transport of *Ag* to the *Ab* can be described by Rath et al. (2012):

$$\frac{\partial C}{\partial t} = D.\nabla^2 C - u.\nabla C$$

(Fick's Law for concentration field of a dilute solvent),

(1)

$$B - \frac{1}{\rho}\nabla.P + \nu.\nabla^2 V = \frac{DV}{Dt}$$

(Navier-Stokes equation (conservation of momentum)), (2)

$$\frac{\partial u}{\partial x} + \frac{\partial v}{\partial y} + \frac{\partial w}{\partial z} = 0 \quad \text{(Continuity equation (conservation of mass))},$$

(3)

$$\frac{d\theta_t}{dt} = K_{\text{on}}C(z=0,x,y,t)\big(\theta_{\max} - \theta_t\big) - K_{\text{off}}\theta_t,$$

(4)

where C is the analyte concentration at time t, D is the diffusivity of the antigens in the solution flowing in the microchannels, u, v, and w are the velocity components in the x, y and z directions, respectively, B is the body force (i.e., due to secondary flows for curved geometries), $\nabla.P$ is the pressure gradient, θ_t is the surface density of antigen–antibody bound complex at time t, $\theta_{\max}$ is the maximum surface density of the immobilized antibodies, and K_{on} and K_{off} are the forward and backward rate constants, respectively, h is the channel height, w is the channel width.

The initial and boundary conditions for the above equations are given by:

$$C(x,y,z,t=0) = 0,$$

(5)

$$u,v,w(t=0) = 0,$$

(6)

$$C_i(x,y,z,t) = C_b \quad (C_b = \text{bulk concentration, at outlet } D_i\nabla C_i = 0),$$

(7)

$$D\frac{\partial C(z=0,x,y,t)}{\partial x} = K_{\text{on}}C(z=0,x,y,t)\big(\theta_{\max} - \theta_t\big) - K_{\text{off}}\theta_t,$$

(8)

$$D\frac{\partial C(z=h,x,y,t)}{\partial x} = 0,$$

(9)

$$D\frac{\partial C(z,x,y=0,t)}{\partial x} = 0,$$

(10)

$$D\frac{\partial C(z,x,y=\text{w},t)}{\partial x} = 0,$$

(11)

$$\theta_t(t=0) = 0.$$

(12)

3 Results and discussion

3.1 Capture efficiencies

3.1.1 Experimental measurements

To study the effect of the secondary flow on the *capture efficiency*, the above-discussed experimental scheme (Sect. 2.3) was utilized for two sets of Ag–Ab, i.e., PSA/anti-PSA (most experiments) and BSA/anti-BSA (limited experiments). We have utilized the CV plot information (peak current, mentioned in Sect. 2.4) to calculate the capture (relative) of PSA in microchannels (straight and serpentine both). A sample CV plot after anti-PSA immobilization and after PSA immobilization for 10 mm serpentine microchannel at 30µL/min is given in Fig. 2a. It clearly illustrates that there is a drop in the peak current after Ag immobilization. Subsequently, the reduction in the peak current to indicate the capture of PSA/anti-PSA as a function of *Re* for the 10 mm long microchannels (straight and one cycle serpentine) and the 20 mm long microchannels (straight and two cycle serpentine) are shown in Fig. 2b and c, respectively. There are three major observations from the figures, (1) the peak reduction in the serpentine channel was greater than that in the straight channel for both the channel lengths, (2) the extent of peak reduction increased with *Re* (i.e., velocity) for both the channel lengths, and (3) for a given velocity and geometry, the longer channel length resulted in a larger overall capture,
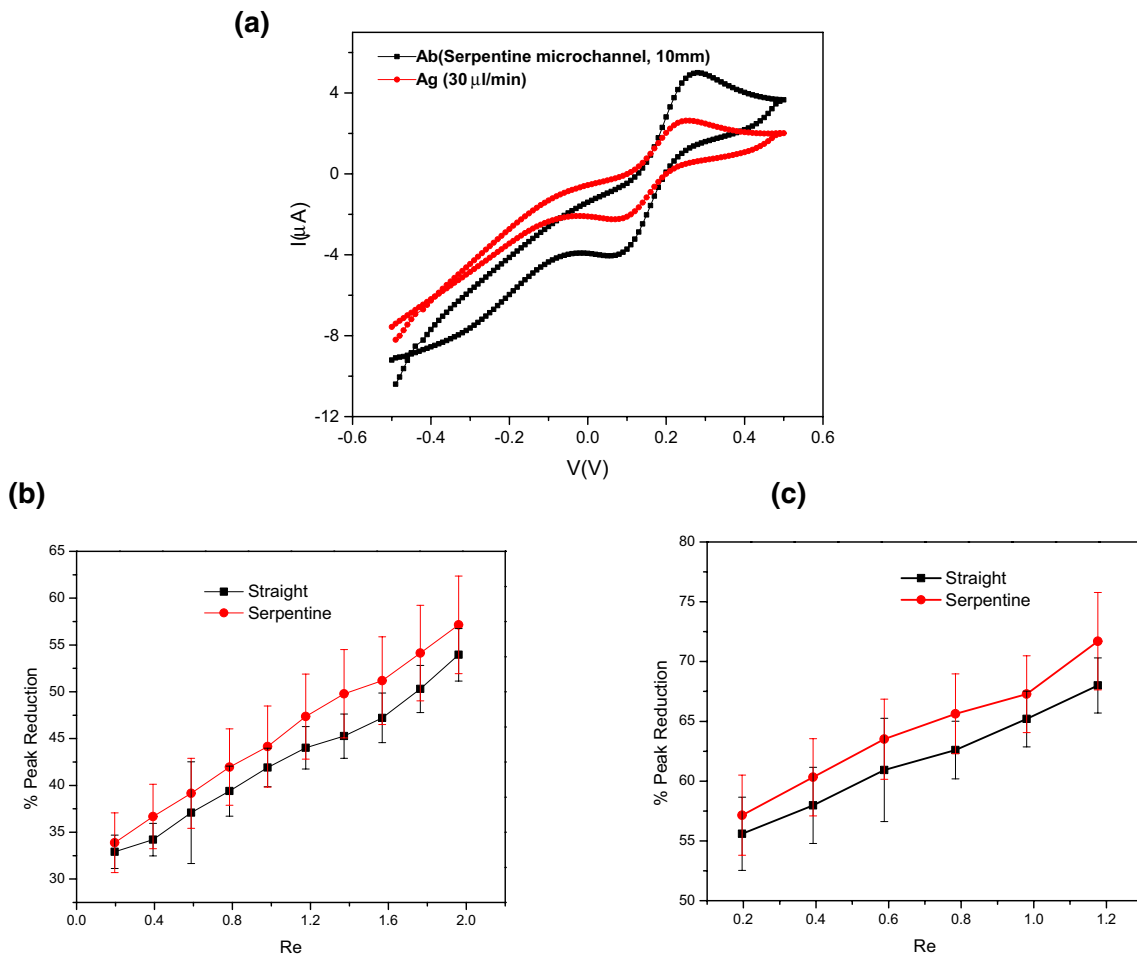
Fig. 2 a The sample CV plot showing the peak current values after Ab–Ag immobilization (at 30 μL/min). Reduction in the peak current with the flow rate for the straight and serpentine glass-PDMS microchannels during capture of PSA by anti-PSA in (**b**) 10 mm long straight and serpentine (1-cycle) microchannels, and **c** 20 mm long straight and serpentine (2-cycle) microchannel

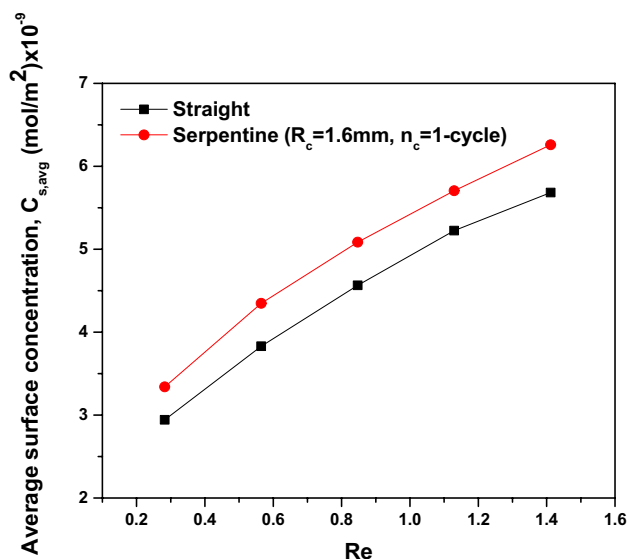but lower capture per unit length. These results are now discussed further.

Regarding the first observation, the higher peak reduction indicates a higher capture of *Ag* in the serpentine channel, which could be attributed to the secondary flows as mentioned. Due to the curved segments in the serpentine geometry, the additional body force is generated whose magnitude can be determined from $\rho v^2/R_c$, where ρ, v, and R_c are the density, velocity of the carrier fluid, R_c is the radius of curvature, respectively. Due to the presence of such forces, the flow profiles were different in the straight and serpentine microchannel, and these are discussed in Sect. 3.1.3. As seen in Fig. 2b at $Re = 1.18$ (30 μL/min), the value of the peak current (Fig. 2a) in the 10 mm long straight channel after anti-PSA immobilization was 5.2628 ± 0.1822 μA, and it reduced to 2.9460 ± 0.0472 μA after the reaction with PSA, corresponding to a reduction of $44.02 \pm 2.26\%$. The peak current for the one cycle serpentine channel after anti-PSA immobilization was 5.0033 ± 0.3211 μA, and it

reduced to 2.6342 ± 0.834 μA after the reaction with PSA, corresponding to a reduction of $47.35 \pm 4.55\%$. The extent of peak reduction was higher for the serpentine channel. For the 20 mm straight channel, the peak currents were 6.3264 ± 0.0941 μA and 2.0241 ± 0.0536 μA after anti-PSA and PSA immobilization, respectively; and for the two cycle serpentine channel, the peak currents were 6.0348 ± 0.1848 μA and 1.7074 ± 0.0627 μA after anti-PSA and PSA immobilization, respectively. Thus, the peak reductions were $68.00 \pm 2.29\%$ and $71.70 \pm 4.07\%$ for the 20 mm straight and the two cycle serpentine channels, respectively; and the extent of the peak reduction was higher for the two cycle serpentine (by ~ 3.70%, with respect to the 20 mm straight microchannel) microchannel. To validate the results of PSA/anti-PSA, limited tests were performed with another Ag–Ab set-BSA/anti-BSA in the 10 mm long channels. At $Re = 0.04$ (1 μL/min), the peak current in the 10 mm straight channel after anti-BSA immobilization was 2.100 ± 0.027 μA and was 1.870 ± 0.041 μA after the BSA

reaction, with the average reduction being $10.95 \pm 0.32\%$. The peak current for the one cycle serpentine channel after anti-BSA immobilization was 1.796 ± 0.0405 µA and was 1.540 ± 0.039 µA after the BSA reaction, with the average reduction being $14.26 \pm 0.58\%$. Thus, similar behaviour was also seen with the BSA/anti-BSA system. No further analysis was performed with the BSA/anti-BSA. Our results of the enhanced capture are supported by the observation of Vijayendran et al. (2003) who, while comparing the initial rates [Fig. 3 (Vijayendran et al. 2003)] for the analyte detection for the reaction between serpentine and straight micro channels, found an enhancement by a factor of two in the serpentine channel; but did not study the effect of other parameters such as the microchannel length, radius of curvature (geometrical parameters) and their effects on the mass transfer coefficient and boundary layer thickness.

Next we discuss the second observation. At a higher flow rate, a higher reduction in the peak current signified an enhancement in the Ab–Ag reaction which could be attributed to the reduction in the thickness of mass transfer boundary layer (detailed information and plot is given in Supplementary Information, Fig. S1). The serpentine channels exhibited even greater enhancement in the capture compared to the straight channels, at a given flow rate, and this attributed to the presence of the additional secondary flow. A similar effect of velocity on the *capture efficiency* was also observed from the simulation study and this will be discussed in Sect. 3.1.2.

Regarding the third observation, we found that more number of antigen molecules were captured in the longer microchannels (both straight and serpentine) but the increase was less than proportionate; i.e., capture per unit length or area decreased with the increasing length or area of the channel. Our results of immunoreaction in the flowing system are supported by our earlier results in non-flow systems (stationary and mixed) (Rath and Panda 2016) where the *capture efficiency* was studied as a function of size of the sensor patch with radius ranging from 0.5 to 3 mm, and the average *capture efficiency* was found to decrease with the area.

3.1.2 Simulation results

We performed numerical simulations to understand, verify and explain the experimental observations. The values of the input parameters were taken from the range defined in the literature (Rath et al. 2012; Rath and Panda 2015a) and are mentioned in Table 1. To calculate the channel length in curved channels, the average of the inner and outer lengths was used.

Figure 3 shows the plots of $C_{s,avg}$ vs. *Re* for the 10 mm long microchannels (both straight and serpentine). It is seen that the $C_{s,avg}$ was more for serpentine microchannel as seen in the experimental results (first observation), which is attributed to the effect of the secondary flow ($\rho v^2 / R_c$) which plays an important role in increasing the analyte *capture efficiency* in the same *Re* range and this aspect is further discussed in Sect. 3.2.1. Due to the presence of the additional force, the velocity profiles near the reacting surface were different in straight and in serpentine microchannel (seen with micro-PIV). Also, it is seen in Fig. 3 that the $C_{s,avg}$ increases with *Re* [as seen in the experimental results, i.e., the second observation)] because a higher velocity reduces the mass transfer boundary layer thickness and increases the mass transfer coefficient (detailed information and plots are given in Supplementary Information, Fig. S1). A similar experimental observation, but in a non-flowing system, of enhanced surface concentration of BSA/anti-BSA, was reported by Rath and Panda (2015a) while increasing the mixing rate. This agrees with our aforementioned experimental observations, mentioned in sub-Sect. 3.1.1 namely that the secondary flow and *Re* affect the *capture efficiency*.

To understand the third observation, we simulated the $C_{s,avg}$ as a function of *Re* for 5 mm and 10 mm serpentine channels having the same radius of curvature (R_c) and the

Fig. 3 Average surface concentration ($C_{s,avg}$, mol/m^2) in the 10 mm long microchannels- straight and 1-cycle serpentine, as a function of the Reynolds Number (*Re*)

Table 1 Input parameters used in the COMSOL simulations

Parameters	Value(s)
K_D	10^{-6} m
K_{on}	10^{+3} m^{-1}s^{-1}
K_{off}	10^{-3} s^{-1}
D_{AB}	3.7×10^{-11} m^2/s
C_b	1.0×10^{-6} mol/m^3
θ_{max}	1.68×10^{-7} mol/m^2

results are shown in Fig. 4. It is seen that the $C_{s,avg}$ (surface density) was higher for the shorter channel length (5 mm), although the total number of molecules captured is more in the longer channel (10 mm). Another important point is regarding the slope of the plot which indicates the enhancement in the *capture efficiency* with *Re*. A shorter channel shows a higher slope, as compared to longer microchannel and hence shorter channel shows a higher extent of enhancement with *Re*. The difference in the $C_{s,avg}$ was also higher at higher *Re* and is attributed to the effect of the secondary flows; the secondary flow term $\left(\frac{\rho v^2}{R_c}\right)$, relates to the square of the velocity and its impact is more at higher velocities.
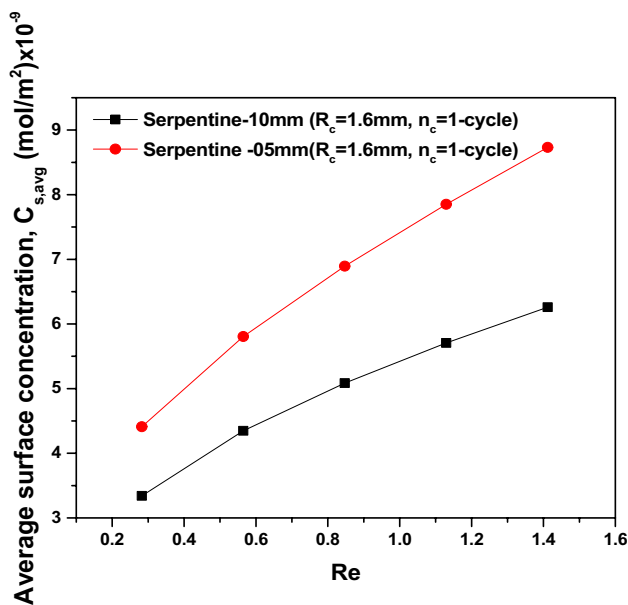

Fig. 4 Simulated values of the average surface concentrations ($C_{s,avg}$) for the 5 mm and 10 mm serpentine microchannels having the same radius of curvature ($R_c = 1.6$ mm)

3.1.3 Micro-PIV experiments and simulations

Figures 5a, b and 6a, b show the experimental and simulated velocity profiles in the mid-plane of the one cycle serpentine microchannel at the region shown as a boxed region in Fig. 1a(ii), at $Re = 1.56$ and 1.95 (flow rates of 40 μL/min and 50 μL/min, respectively). Validation of the no-slip condition was done experimentally; and similar observations of the no-slip condition for micro-PIV were also reported by Meinhart et al. (1999) and Zheng and Silber (2008). The streamlines in the Figs. 5 and 6 showed the direction of flow field, and the change in the magnitude of the velocity from the outer wall to the inner wall (i.e., radially inward). We also compared the nature of the flow profile at (40 μL/min) $Re = 1.56$ at the mid plane, which has the minimum shear stress and the maximum velocity. The velocity ranged from 0 to 0.0261 m/s in the simulation and from 0 to 0.0300 m/s in the experiment. We also performed the experiment at different locations and at different planes along the flow and found good agreement between the experimental and the simulation results. The results from the micro-PIV studies match the nature and magnitude of the flow profiles obtained from the experiments and the numerical simulations, and clarifies the role of curved section in alteration of flow profile, which is the primary reason for *capture efficiency* enhancement in serpentine microchannels. As the flow rate varies, the shear stress and shear rate changes. In this study the shear stress varied from 0.2937 N/m² (0.5 cycle, $Re = 0.282$) to 1.4078 N/m² (2 cycle, $Re = 1.41$). Shear rate varies with geometry as well as with flow rate.

3.2 Parametric study of the secondary flow

In the earlier section, we saw that the higher peak reduction or higher analyte capture in a serpentine channel compared to a straight channel was attributed due to the presence of a
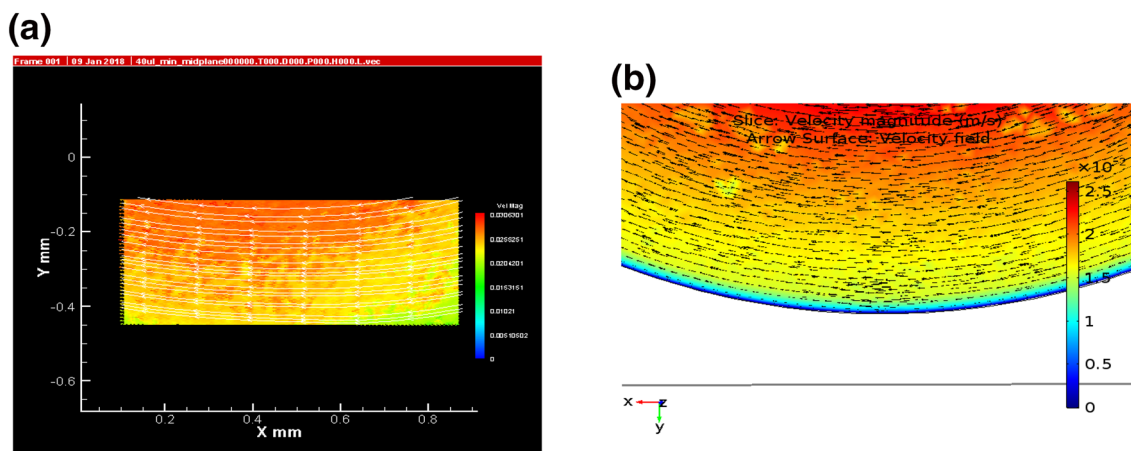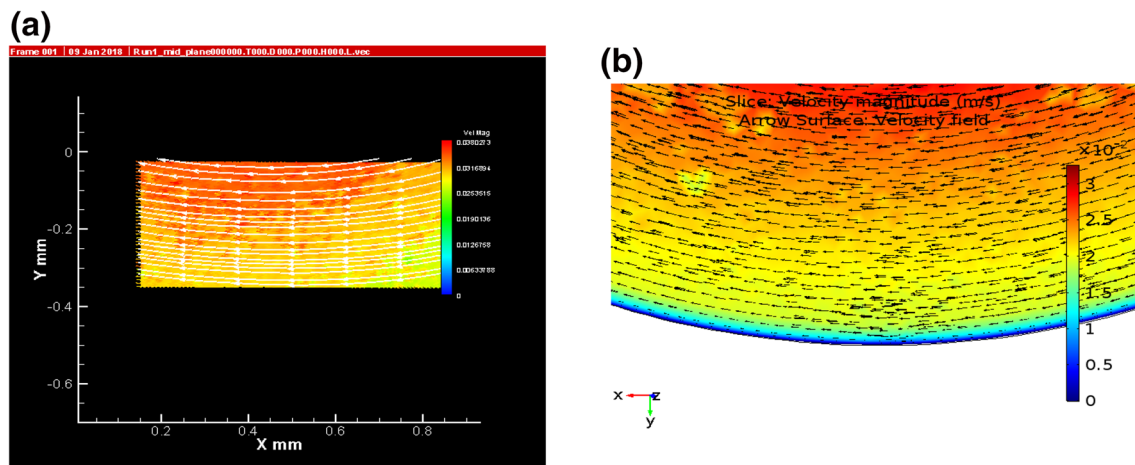

Fig. 5 Flow profile in the mid-plane at $Re = 1.56$ (40 μL/min flow rate). **a** Micro-PIV profile, and **b** simulated profile

(a)

(b)

Fig. 6 Flow profile in the mid-plane at $Re = 1.95$ (50 µL/min flow rate). **a** Micro-PIV profile, and **b** simulated profile

secondary flow which changes the velocity profile near the reactive surface and enhances the mass transport leading to a higher extent of reaction. Therefore, it is necessary to analyze further the process and geometrical parameters that have a major impact on the capture of a target analyte, i.e., Ag by the immobilized species (Ab) on the microchannel surface. An increased flux will result in more analyte being captured and lead to a lower (improved) limit of detection (LOD). In this section, the variation of process and geometrical parameters were studied using numerical simulations to understand the effect of the parameters on the analyte capture, which may not be possible due to experimental limitations. Moreover, a controlled parametric study of the influence of individual parameters on the analyte capture has been attempted and the outcome of parameters like total molar flux and co-relations between *capture efficiency* and *De* are investigated in detail.

3.2.1 Effect of *Re*/velocity and radius of curvature (R_c)

To understand the effect of the process parameter of interest (carrier fluid velocity here), the *Re* was varied in the range 0.282–1.41 (values taken from the experiments); and for the geometrical parameters (radius of curvature and channel length), microchannels of lengths 5 mm and 10 mm were used. For different radii of curvature (R_c), the microchannel of 10 mm length was cast in the shape of a semi-circle, 2 semi-circles, 3 semi-circles and 4 semi-circles, which are termed here as 0.5-cycle, 1-cycle, 1.5-cycle and 2-cycles, respectively (n_c-number of cycles, $n_c > 2$ were not possible and the relevant images are shown in Supplementary Information, Fig. S5). R_c decreases as the number of cycles increases. The channel width and height were the same as used for the experiments. For all the serpentine microchannels, the $C_{s,avg}$ is plotted as a function

of *Re* in Fig. 7a and as a function of R_c (for $Re = 0.282$ and $Re = 1.41$) in Fig. 7b.

With regards to the effect of *Re*, it is observed from Fig. 7a that for the given serpentine microchannel the $C_{s,avg}$ increases monotonically with *Re* for all the cases. A similar behaviour was observed in Sect. 3.1.1 while comparing the experimental values of the analyte capture in the straight and the serpentine microchannels. This is attributed to the enhanced *capture efficiency* with increased velocity due to the presence of the force due to secondary flows ($\rho v^2 / R_c$), and the reduced boundary layer thicknesses.

With regards to the effect of R_c, the higher $C_{s,avg}$ is observed with more number of cycles present in the serpentine microchannel (Fig. 7a). The extent of analyte capture was even higher at higher velocity due to the quadratic nature of velocity dependence on the force. Figure 7b compares the analyte *capture efficiency* as a function of R_c at fixed *Re* (i.e., at a constant velocity). The extent of analyte capture increases with decrease in R_c. The extent of capture was even higher when a smaller R_c was coupled with a higher value of *Re*.

We obtained the average molar flux using numerical simulations and it provides the mass transfer coefficient (K_c). The mass transfer boundary layer also evolves during the flow and reaction. To compute the boundary layer thickness (δ_m) with the mass transfer coefficient, the film model equation shown below was used:

$$K_c = \left(D_{AB} / \delta_m \right). \tag{13}$$

Figure 8a compares the average molar flux for all the 10 mm long serpentine microchannels ($n_c = 0.5$–2 cycles, variable R_c) as a function of *Re* and Fig. 8b for the 5 mm and 10 mm long serpentine microchannels as a function of *Re* (having a fixed R_c of 1.6 mm).
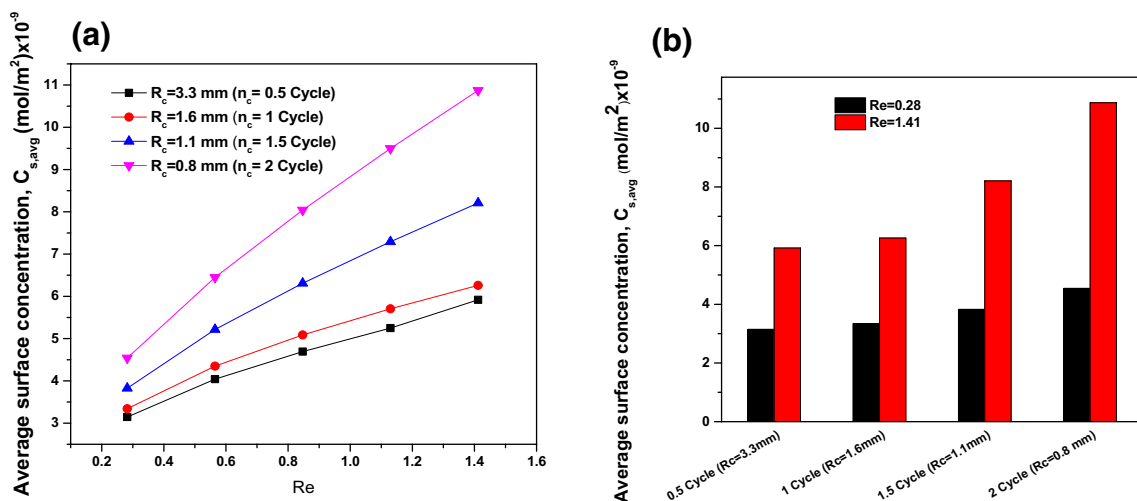
Fig. 7 Simulated average surface concentration ($C_{s,\text{avg}}$) for all serpentine microchannels ($n_c = 0.5$–2-cycles) **a** as a function of Re and **b** as a function of the radius of curvature (R_c)

From Fig. 8a, we have three observations, (1) the average molar flux increases with increase in Re, (2) the average molar flux increases with decrease in R_c, and (3) the increase in the average molar flux per unit Re is more at lower values of R_c. With increase in Re (velocity), the inertial forces increase and the decrease in R_c enhances the extent of the secondary flow which reduces the boundary layer thickness and results in a higher molar flux. The decrease in the boundary layer thickness, (with increased Re and decreased R_c, details are given in Supplementary Information, Fig. S1) accounts for the enhanced mass transfer coefficient. A similar behaviour was observed for all serpentine microchannels. At $Re = 0.282$, the average molar flux varies from

3.326×10^{-12} mol/m^2 s ($n_c = 0.5$ cycle) to 4.785×10^{-12} mol/m^2 s ($n_c = 2$ cycle) and at $Re = 1.41$, it varies from 6.190×10^{-12} mol/m^{2}s ($n_c = 0.5$ cycle) to 11.995×10^{-12} mol/m^2 s. The enhancements are 43.86% and 93.78%, respectively. The serpentine microchannel with two cycles shows the maximum capture among all cases. This also verified our first and second experimental observations (Sect. 3.1.1), i.e. the effect of Re and secondary flows on the surface reaction.

Figure 8b, confirms the third observation of the Sect. 3.1.1 (For the 10 and 20 mm long microchannels), that how the microchannel length affects the $C_{s,\text{avg}}$. For shorter channels, the higher molar flux leads to higher analyte surface density; and thus, the shorter channel had higher enhancement
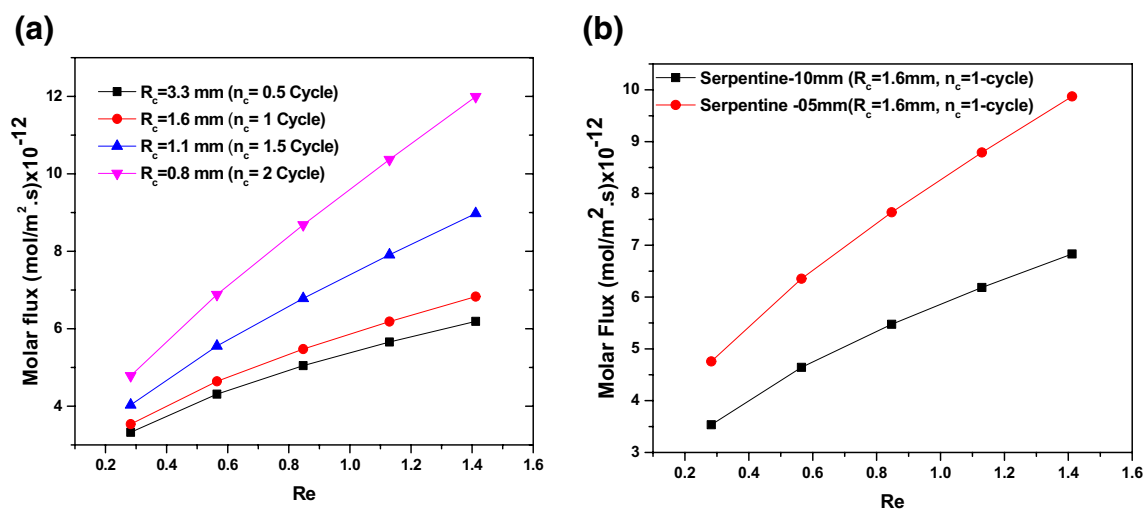
Fig. 8 The average molar flux, **a** for all serpentine microchannels as a function of Re (fixed length and variable R_c), **b** for 1-cycle serpentine microchannel as a function of Re (variable length and fixed R_c)

with Re and a smaller boundary layer thickness (details are given in Supplementary Information, Fig. S2). At $Re = 0.282$, the average molar flux varies from 3.535×10^{-12} mol/m²s $(l = 10$ mm$) - 4.757 \times 10^{-12}$ mol/m²s$(l = 5$ mm$)$, and at $Re = 1.41$, it varies from 6.830×10^{-12} mol/m²s$(l = 10$mm$)$ -9.873×10^{-12} mol/m²s$(l = 5$ mm$)$. Here the enhancements are 34.57% and 44.55%, respectively. In conclusion, in the former part of this section, we have shown the effect of R_c and Re at constant length. In the latter part, we have shown the effect of channel length and Re at constant R_c on the molar flux. To get the same amount of analyte capture (or molar flux), different combinations of Re and R_c can be used and this gives more choices and flexibility to the designer.
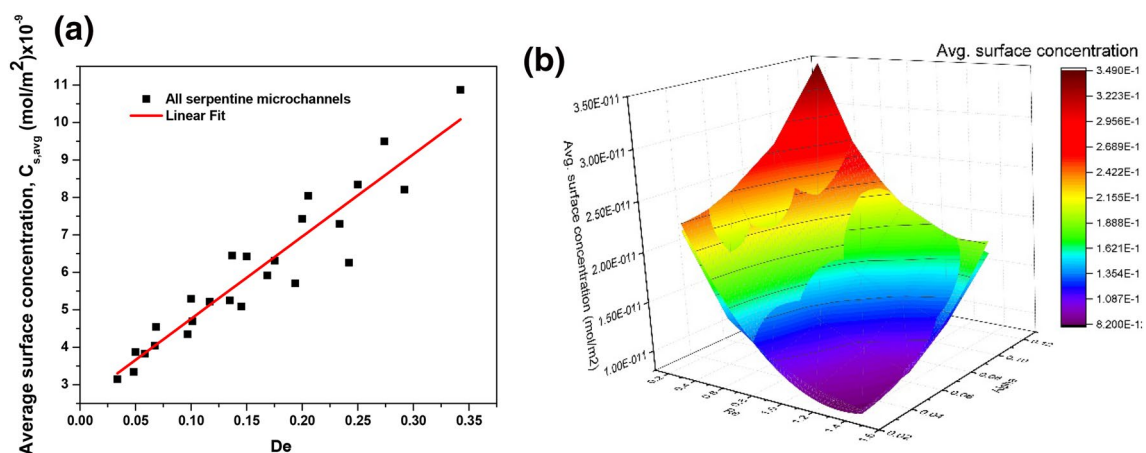
3.2.2 Co-relations

To explore the possibility of a co-relation between the $C_{s,\text{avg}}$ and De (which accounts for the process and geometrical parameters shown in Fig. 9a), the $C_{s,\text{avg}}$ of all serpentine microchannels were plotted as a function of De and fitted linearly. The obtained linear function ($R^2 = 0.89$) is:

$$C_{s,\text{avg}} = 2.56 \times 10^{-9} + 21.97 \times 10^{-9} \times De.$$

To obtain a more detailed co-relation, we extended our analysis and split De as a function of Re and α, and plotted the $C_{s,\text{avg}}$ as a function of Re and α, on the 3D plot shown in Fig. 9b. The co-relation is as follows:

$$\begin{aligned} C_{s,\text{avg}} = {} & 3.281 \times 10^{-11} - 3.854 \times 10^{-11} \\ & \times Re - 4.498 \times 10^{-11} \times \alpha + 1.499 \times 10^{-11} \\ & \times Re^2 + 1.079 \times 10^{-09} \times \alpha^2. \end{aligned}$$
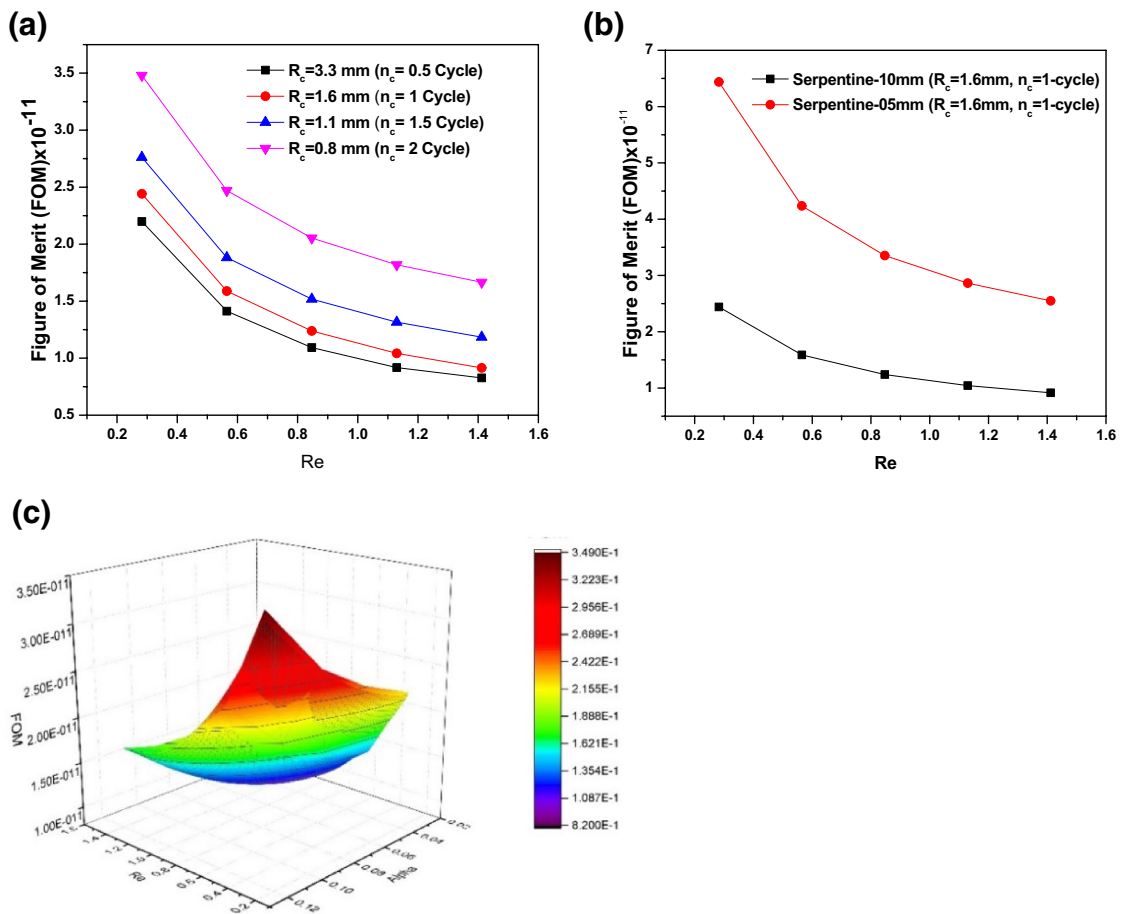
From the above co-relation we can see that α, which governs the secondary flow has a relatively higher impact on the $C_{s,\text{avg}}$. This knowledge could provide more relevant information to the process designer.

3.3 Figure of merit

The *figure of merit* (*FOM*) is defined here as the ratio of the $C_{s,\text{avg}}$ (the desired performance) to the pressure drop (energy expended or cost) due to fluid flow. With the 10 mm long microchannel, we have examined up to two cycles (more cycles were not possible). In this section we have analyzed the *FOM* values with respect to the process and the geometric parameters. In Fig. 8a and b, we had plotted the molar flux values for all 10 mm long serpentine microchannels as a function of Re for a microchannels with constant length (with variable R_c) and for constant R_c (with variable length), respectively. Here, the *FOM* as a function of Re for a constant length (with variable R_c) and for a constant R_c (with variable length), are presented in Fig. 10a and b, respectively. There are three observations−Fig. 10a and b, (1) the *FOM* decreases monotonically (although both the $C_{s,\text{avg}}$ and the pressure drop increase) with increase in Re (2) the *FOM* increases with decrease in R_c, and (3) the *FOM* is higher for shorter channels of same R_c. Similar monotonic reductions in a *FOM* with Re have been reported by Mandal et al. (2010) (where the FOM is defined as the ratio of the heat transfer enhancement per unit pumping power by the system) and Mandal et al. (2011) (where the *FOM* is defined as the ratio of the unmixedness of liquid in a system per unit pumping power by the system) in their heat transfer investigations using secondary flows.

We plotted the *FOM* values as a function of Re and α, shown in Fig. 10c, and obtained a co-relation:

Fig. 9 **a** Simulated average surface concentration ($C_{s,\text{avg}}$) for all serpentine microchannels ($n_c = 0$–2) as a function of De. **b** Simulated average surface concentration ($C_{s,\text{avg}}$) of all serpentine microchannels ($n_c = 0$–2) as a function of Re and n_c

(a)

(b)

(c)

Fig. 10 **a** Figure of merit (FOM) for all serpentine microchannels as a function of *Re*. **b** Figure of merit (FOM) as a function of Re for 5 mm and 10 mm serpentine microchannels. **c** Figure of merit (FOM) for all serpentine microchannels studied in this work as a function of *Re* and α

$$FOM = 3.038 \times 10^{-11} - 3.567 \times 10^{-11}$$
$$\times Re - 1.156 \times 10^{-11} \times \alpha + 1.499 \times 10^{-11}$$
$$\times Re^2 + 1.079 \times 10^{-09}$$
$$\times \alpha^2 - 3.945 \times 10^{-11} \times Re \times \alpha.$$

This co-relation could provide more choices to the designer. More information regarding Fig. 10c is provided in the video in the Supplementary Information (SI-Video).

4 Conclusions

We performed experiments to study the effects of the channel geometry [radius of curvature (R_c), channel length (*l*)] and process conditions (*Re* representing the flow velocity) on the capture of antigens by the surface immobilized antibodies in the straight and the serpentine microchannel-based heterogeneous immunosensors and observed the role of secondary flows. There were three major observations: (1) higher analyte capture in the serpentine channel than that in the straight channel for all the channel lengths, (2) the extent of analyte capture increased with *Re* (i.e., velocity) for all the channel lengths, and (3) for a given velocity and geometry, the longer channel length resulted in a larger overall analyte capture, but with lower capture per unit length. The experimental observations were explained using numerical simulations. For more detailed understanding of the phenomena, we conducted micro-PIV studies at different planes and sections of the serpentine microchannels and matched the results with the simulated velocity profiles. Then, using numerical simulations, we conducted a parametric study of the process and the geometrical parameters and further investigated the effect of these parameters on analyte capture through the behaviour of the average molar flux, boundary layer thickness, mass

transfer coefficients as functions of Re and R_c. A highlight of the work is a correlation of the average surface concentration as a function of the De, which is further elaborated by the correlation with the constituents of the De (i.e. Re and α). Finally, we plotted FOM for the different conditions studied and formulated a correlation for FOM as a function of Re and α. The scientific investigations of the geometrical and process parameters affecting the analyte capture and the engineering correlations proposed will be useful in the designing more efficient flow-based heterogeneous immunosensors.

References

Art MS, Noblitt SD, Krummel AT et al (2018) IR-compatible PDMS microfluidic devices for monitoring of enzyme kinetics. Anal Chimica Acta 1021:95–102

Bange A, Halsall B, Heineman WR (2005) Microfluidic immunosensor systems. Biosens Bioelectron 20:2488–2503

Bhuvana M, Narayanan JS, Dharuman V et al (2013) Gold surface supported spherical liposome–gold nano-particle nano-composite for label free DNA sensing. Biosens Bioelectron 41:802–808

Brown AP, Anson FC (1977) Cyclic and differential pulse voltammetric behavior of reactants confined to the electrode surface. Anal Chem 49:1589–1595

Chauhan R, Singh J, Solanki PR (2016) Label-free piezoelectric immunosensor decorated with gold nanoparticles: kinetic analysis and biosensing application. Sens Actu B 222:804–814

Chen S et al (2019) microfluidic device directly fabricated on screen-printed electrodes for ultrasensitive electrochemical sensing of PSA. Nano Res Let 14:71

Chepyala R, Panda S (2013) Tunable surface free energies of functionalized molecular layers on Si surfaces for microfluidic immunosensor applications. App Surf Sci 271:77–85

Chepyala R, Panda S (2014) Zeta potential and Reynolds number correlations for electrolytic solutions in microfluidic immunosensor. Micro Nano 18:1329–1339

Di CM, Ting YY, Yang DZ et al (2019) Microchannel with stacked microbeads for separation o Plasma from whole blood. Chinese J Anal Chem 47(5):661–668

Dravid AN, Smith KA, Merrill EW, Brian PLT (1971) Effect of secondary fluid motion on laminar flow heat transfer in helically coiled tubes. AlChE J 17:1114–1122

Foley JO, Hossein AM, Fu E et al (2008) Experimental and model investigation of the time-dependent 2-dimensional distribution of binding in a herringbone microchannel. Lab Chip 8:557–564

Fujii T (2002) PDMS-based microfluidic devices for biomedical applications. Micro Electron Eng 61–62:907–914

Golden JP, Floyd-Smith TM, Rott DR et al (2007) Target delivery in a microfluidic immunosensor. Biosens Bioelectron 22:2763–2767

Hessel V, Lowe H, Schonfeld F (2005) Micromixers—a review on passive and active mixing principles. Chem Engg Sci 60:2479–2501

Hu G, Gao Y, Li D (2007) Modeling micropatterned antigen-antibody binding kinetics in a microfluidic chip. Biosens Bioelectron 22:1403–1409

Ibii T, Kaieda M, Hatakeyama S et al (2010) Direct immobilization of gold-binding antibody fragments for immunosensor applications. Anal Chem 82:4229–4235

Imran H, Manikandan PN, Prabhu D et al (2019a) Ultra selective label free electrochemical detection of cancer prognostic p53-antibody at DNA functionalized grapheme. Sens Bio-sens Res 23:100261

Imran H, Manikandan PN, Dharuman V (2019b) Ultra-sensitive and selective label free electrochemical DNA detection at layer-by-layer self-assembled graphene oxide and vesicle liposome nano-architecture. J Electro Anal Chem 835:10–21

Jeon W, Shin BC (2009) Design and simulation of passive mixing in microfluidic systems with geometric variations. Chem Engg J 152:575–582

Kadilak AL, Ying L, Shrestha S et al (2014) Selective deposition of chemically- bonded gold electrodes onto PDMS microchannel side walls. J Electroanal Chem 727:141–147

Kalita P, Singh J, Singh MK et al (2012) Ring like self-assembled Ni nanoparticles based biosensor for food toxin detection. Appl Phy Let 100:093702

Kirtland JD, McGraw GJ, Stroock AD (2006) Mass transfer to reactive boundaries from steady three-dimensional flows in microchannels. Phys Fluids 18:073602-1-13

Klink MJ, Iwuoha EI, Ebenso EE (2011) The electro-catalytic and redox-mediator effects of nanostructured PDMA-PSA modified-electrodes as phenol derivative sensors. Int J Electrochem Sci 6:2429–2442

Kumar V, Paraschivoiu M, Nigam KDP (2011) Single-phase fluid flow and mixing in microchannels. Chem Eng Sci 66:1329–1373

Lebedev K, Mafe S, Stroeve P (2006) Convection, diffusion and reaction in a surface-based biosensor: modeling of cooperativity and binding site competition on the surface and in the hydrogel. J Colloid Int Sci 296:527–537

Li N, Schwartz M, Zanetti CI (2009) PDMS compound adsorption in context. J Biomol Screen 14(2):194–202

Lynn NS, Homola JJ (2015) Biosensor enhancement using grooved micromixers: Part I, numerical studies. Anal Chem 87:5516–5523

Lynn NS, Sipova H, Adam P, Homola JJ (2013) Enhancement of affinity-based biosensors: effect of sensing chamber geometry on sensitivity. Lab Chip 13:1413–1421

Lynn NS, Lopez JIM, Bockova M et al (2014) Biosensing enhancement using passive mixing structures for microarray-based sensors. Biosens Bioelectron 54:506–514

Lynn NS, Bockova JM, Adam P, Homola J (2015) Biosensor enhancement using grooved micromixers: Part II, experimental studies. Anal Chem 87:5524–5530

Mandal MM, Kumar V, Nigam KDP (2010) Augmentation of heat transfer performance in coiled flow inverter vis-a-vis conventional heat exchanger. Chem Eng Sci 65:999–1007

Mandal MM, Aggarwal P, Nigam KDP (2011) Liquid-liquid mixing in coiled flow inverter. Ind Eng Chem Res 50:13230–13235

Meinhart CD, Wereley ST, Santiago JG (1999) PIV measurements of a microchannel flow. Exp Fluids 27:414–419

Meng-Di C et al (2019) Microchannel with stacked microbeads for separation of plasma from whole blood. Chin J Anal Chem 47(5):661–668

Nelson KE, Foley JO, Yager P (2007) Concentration gradient immunoassay. 1. An immunoassay based on interdiffusion and surface binding in a microchannel. Anal Chem 79:3542–3548

Rath D, Panda S (2015a) Enhanced capture efficiencies of antigens in immunosensors. Chem Eng J 60:657–670

Rath D, Panda S (2015b) Contribution of rotational diffusivity towards the transport of antigens in heterogeneous immunosensors. Analyst 140:6579–6587

Rath D, Panda S (2016) Correlation of capture efficiency with the geometry, transport, and reaction parameters in heterogeneous immunosensors. Langmuir 32:1410–1418

Rath D, Kumar S, Panda S (2012) Enhancement of antigen–antibody kinetics on nanotextured silicon surfaces in mixed non-flow systems. Mat Sci Eng C 32:2223–2229

Reverberi R, Reverberi L (2007) Factors affecting the antigen-antibody reaction. Blood Transfus 5:227–240

Singh J, Kalita P, Singh MK et al (2011) Nanostructured nickel oxide-chitosan film for application to cholesterol sensor. Appl Phy Let 98:123702

Solanki PR, Kaushik A, Ansari AA et al (2008) Zinc oxide-chitosan nanobiocomposite for urea sensor. Appl Phys Let 93:163903

Squires TM, Messinger RJ, Manalis SR (2008) Making it stick: convection, reaction and diffusion in surface-based biosensors. Nat Biotechnol 26:417–426

Srivastava S et al (2011) A self assembled monolayer based microfluidic sensor for ures detection. Nanoscale 3:2971–2977

Vijayendran RA, Leckband DE (2001) A quantitative qssessment of heterogeneity for surface-immobilized proteins. Anal Chem 73:471–480

Vijayendran RA, Motsegood KM, Beebe DJ, Leckband DE (2003) Evaluation of a three-dimensional micromixer in a surface-based biosensor. Langmuir 19:1824–1828

Wang S, Liu K, Liu J (2011) Highly efficient capture of circulating tumor cells by using nanostructured silicon substrates with integrated chaotic micromixers. Angew Chem Int Ed 50:3084–3088

Zhang F et al (2015) A microfluidic love-wave biosensing device for PSA detection based on an Aptamer Beacon Probe. Sensors 15:13839–13850

Zhang D, Ma J, Meng X et al (2019) Electrochemical aptamer-based microsensor for real-time monitoring of adenosine in vivo. Anal Chim Acta 1076:55–63

Zheng X, Silber ZH (2008) Measurement of velocity profiles in a rectangular microchannel with aspect ratio $\alpha = 0.35$. Exp Fluids 44:951–959